

Direct observation of Dirac cones and a flatband in a honeycomb lattice for polaritons

T. Jacqmin,¹ I. Carusotto,² I. Sagnes,¹ M. Abbarchi,¹ D. D. Solnyshkov,³
G. Malpuech,³ E. Galopin,¹ A. Lemaître,¹ J. Bloch,¹ and A. Amo¹

¹*Laboratoire de Photonique et Nanostructures, CNRS/LPN, Route de Nozay, 91460 Marcoussis, France*

²*INO-CNR BEC Center and Dipartimento di Fisica, Università di Trento, I-38123, Povo, Italy*

³*Institut Pascal, PHOTON-N2, Clermont Université, Université Blaise Pascal, CNRS, 24 avenue des Landais, 63177 Aubière Cedex, France*

(Dated: October 25, 2018)

Two-dimensional lattices of coupled micropillars etched in a planar semiconductor microcavity offer a workbench to engineer the band structure of polaritons. We report experimental studies of honeycomb lattices where the polariton low energy dispersion is analogous to that of electrons in graphene. Using energy resolved photoluminescence we directly observe Dirac cones, around which the dynamics of polaritons is described by the Dirac equation for massless particles. At higher energies, we observe p orbital bands, one of them with the non-dispersive character of a flat band. The realization of this structure which holds massless, massive and infinitely-massive particles opens the route towards studies of the interplay of dispersion, interactions and frustration in a novel and controlled environment.

PACS numbers: 71.36.+c, 78.67.-n, 42.65.Tg, 73.22.Pr

Engineering Hamiltonians in controlled systems has proven to be a useful tool to simulate and unveil complex condensed matter phenomena otherwise experimentally inaccessible. Indeed, condensed-matter systems usually lack of control and observables, whereas model systems such as ultra-cold atoms [1], arrays of photonic waveguides [2], or polariton gases [3] enable the control of the density, the temperature and, in the case of lattice systems, the topology of the band structure. In this context, a system that has attracted a lot of attention is the honeycomb lattice, whose geometry is responsible for the transport properties of graphene. This extraordinary material [4] shows point-like intersections between the conduction and valence bands. Around those points, usually referred to as Dirac points, the energy dispersion is linear, and electrons behave like massless relativistic particles [5]. The honeycomb geometry gives rise to intriguing phenomena such as anomalous Klein tunneling [6] and geometric phase effects that result in the antilocalization of electrons [7].

The investigation of this physics has triggered the realization of simulators [8] whose parameters can be controlled in a range not easily accessible in graphene. For instance, in the field of cold atoms, honeycomb optical lattices were realized [9, 10], while in solids honeycomb lattices for electrons were created by nanopatterning a two-dimensional electron gas [11] and by molecule-by-molecule assembly on metal surfaces using scanning probe methods [12]. In photonics, light induced lattices in non-linear crystals [13], arrays of coupled waveguides [14, 15] and resonators were used in an hexagonal geometry [16, 17]. While these systems have shown remarkable features like topological phase transitions [10] or the possibility of including synthetic gauge fields [14], they lack simultaneous control of the particle momen-

tum, local potential, interactions and on-site visualization. In this sense, polaritons in semiconductor planar microcavities appear as an extraordinary platform overcoming these limitations [3]. These light-matter particles arise from the strong coupling between cavity photons and quantum well excitons, and can be created, manipulated, and detected using optical techniques. Two-dimensional lattices for polaritons have been implemented using surface acoustic waves [18, 19] and gold deposition at the surface of the cavity [20–22]. However, the former method allows very limited lattice geometries, while the latter can only provide very shallow modulations of the potential: both limitations strongly restrict the new physics that can be studied in these systems. On the other hand, the recent realization of coupled micropillars based on deep etching of a planar structure [23, 24] has opened the way towards the engineering of lattices for polaritons with controlled tunneling and deep on-site potentials with arbitrary geometry.

In this letter, we report on a honeycomb lattice for polaritons, made of hundreds of coupled micropillars etched in a planar semiconductor microcavity. By monitoring the photoluminescence at low excitation density, we image the energy dispersion of the structure, which consists in several energy bands. The lowest two arise from the coupling between the fundamental modes of the micropillars. They are analogous to the π and π^* bands of graphene [5]. In particular we directly evidence six Dirac cones at the corners of the first Brillouin zone, around which the energy dispersion is linear. When increasing the excitation intensity, we observe polariton condensation occurring at the top of the π^* band, at zero Bloch momentum (Γ symmetry point), showing spatial coherence extended over the whole excitation spot. Additionally, we report on the presence of higher energy bands

arising from the coupling between higher energy modes of the pillars. In particular, we observe a non dispersive band in which polaritons have an infinite effective mass. The observation of this flat band, first predicted in the context of cold atomic gases, opens the way to the study of the interplay of interactions, frustration and spin dynamics in a novel driven-dissipative framework.

Our structure is a $Q = 72000 \lambda/2$ microcavity. It is made of a $Ga_{0.05}Al_{0.95}As$ layer surrounded by two $Ga_{0.05}Al_{0.95}As/Ga_{0.8}Al_{0.2}As$ Bragg mirrors with 28/40 top/bottom pairs respectively. Twelve GaAs quantum wells of 7 nm width are inserted inside the cavity, resulting in a Rabi splitting of 15 meV. Experiments are performed at 10 K and -17 meV cavity-exciton detuning. We engineer a honeycomb lattice of coupled micropillars by using electron beam lithography and dry etching of the sample down to the GaAs substrate (see scanning electron microscope image of the structure in Fig. 1(a)). The diameter of each micropillar is $d = 3 \mu\text{m}$, and the distance between two adjacent micropillars, which defines the lattice constant, is $a = 2.4 \mu\text{m}$. In those conditions, the etched cavity shows a polariton lifetime of 27 ps at the bottom of the lower polariton band. As the interpillar distance is smaller than their diameter, the micropillars spatially overlap (see sketch in Fig. 1(b)). This results in a sizable polariton tunnel coupling between adjacent micropillars [24] via their photonic component. For our structure, the tunnel coupling amounts to 0.25 meV. The system is excited out of resonance with a Ti:Sapph monomode laser at the energy of the first reflectivity minimum of the stop band (1.687 eV) in a spot of $30 \mu\text{m}$ diameter covering around 30 micropillars. The photoluminescence is collected through a high numerical aperture objective (NA = 0.65), dispersed in a spectrometer and detected by a CCD camera on which we can image either the real or the momentum space. Note that we use a low-bandpass filter to avoid the laser stray light in the detector, and that a chopper was used in the case of high power excitation to avoid heating of the sample.

Under non-resonant, low power excitation, the incoherent relaxation of polaritons results in the population of all the energy bands of the structure. Note that for low power excitation polariton-polariton interactions are negligible so that single particle physics of the honeycomb lattice is probed. Figure 1(d) shows the measured far field photoluminescence containing many groups of bands, separated by energy gaps. The two lowest bands (S bands) arise from the coupling between the fundamental mode of the pillars, which is a cylindrically symmetric (S) mode. At higher energy, we observe a group of four bands (P bands) arising from the coupling between the first excited state of the pillars, which is twice degenerate and has two lobes [24], as sketched in Fig. 1(e). The separation between these two groups of bands is $\Delta E = 3.2 \text{ meV}$, the energy difference between the two

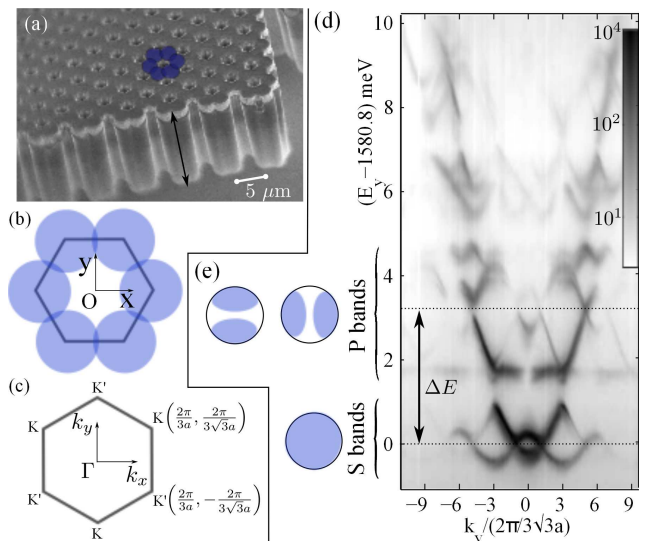


FIG. 1. a) Scanning electron microscope image of a corner of the microstructure. One hexagon of pillars is underlined with blue disks. The dark arrows show the growth axis of the cavity. The overlap between pillars is sketched in (b). (c) Reciprocal space (first Brillouin zone) showing the Γ symmetry point at the center of the zone and Dirac K and K' symmetry points at its corners. (d) Measured momentum space energy resolved photoluminescence along the $k_x = 2\pi/3a$ line, under non-resonant low power excitation. (e) Sketch of the real space distribution of S and P modes in a single pillar.

lowest energy states of the individual pillars. Above those two groups of bands, many other can be seen arising from the hybridization of higher energy modes of the pillars.

We first concentrate on the two S bands. They stem from the coupling between micropillar states which have a cylindrical symmetry similar to that of the carbon P_z electronic orbitals in graphene. Thus, we expect the two S bands to present features analogous to the π and π^* bands of graphene, including six Dirac (contact) points [5] in the first Brillouin zone (sketched in Fig. 1(c)). Figure 2(a) shows the measured emitted intensity in momentum space when only the energy of the Dirac points is selected (zero energy in Fig. 1(d)). We observe the six Dirac points at the corner of the first Brillouin zone (yellow points). The adjacent Brillouin zones are also seen. Figure 2(b, c) show the measured energy resolved emission along the lines 1 and 2 indicated in Fig. 2(a), passing through four and three Dirac linear intersections respectively. As the confinement energy on each site of the lattice is much larger than the tunneling energy, the system is well described by the tight binding approximation. Including first and second neighbor tunneling the following dispersion can be obtained [5]:

$$E(\mathbf{k}) = \pm t \sqrt{3 + f(\mathbf{k})} - t' f(\mathbf{k}), \quad (1)$$

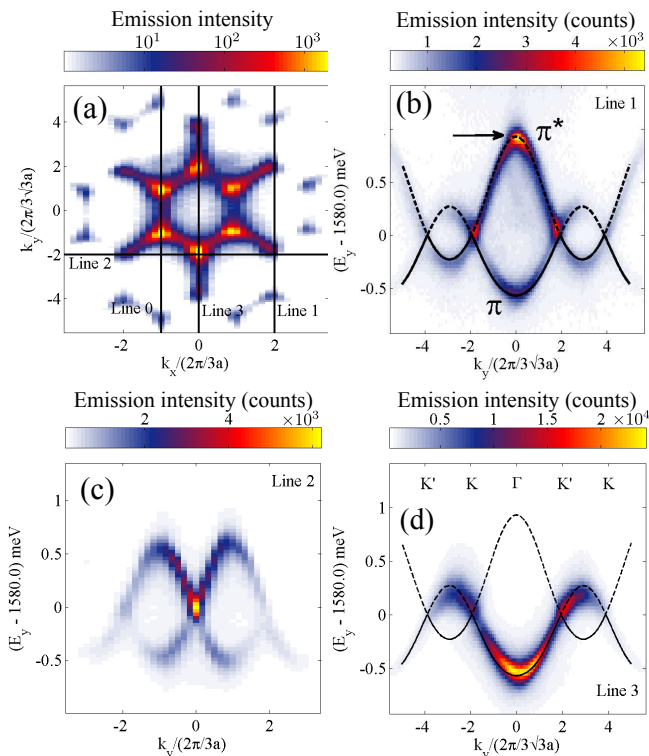


FIG. 2. (a) Measured photoluminescence intensity in momentum space at the energy of the Dirac points (dotted line in Fig.1(d)). (b) Spectrally resolved far field emission along line 1 in (a). The black line is a fit to Eq. 1. (c) Same as (b) along line 2 in (a). (d) Spectrally resolved far field emission along line 3 in (a), passing through the first Brillouin zone.

where

$$f(\mathbf{k}) = 2 \cos(\sqrt{3}k_y a) + 4 \cos\left(\frac{\sqrt{3}}{2}k_y a\right) \cos\left(\frac{3}{2}k_x a\right). \quad (2)$$

By fitting Eq. 1 to the data in Fig. 2 we extract a value of the coupling between first and second neighbors of $t = 0.25$ meV and $t' = -0.02$ meV respectively. The result of the fit is shown in Fig. 2(b), giving a Fermi velocity of $v_F = \sqrt{3}at/2\hbar = 1.3 \times 10^7$ m.s $^{-1}$. Note that the photoluminescence profile shown in Fig. 2(b) does not belong to the first Brillouin zone (Bz). If we perform the same measurement through the first Bz, (along line 3 in Fig. 2(a)), we observe that the emission is absent in the upper band (π^*) within the first Bz, and in the lower band (π) within the second Bz (see Fig. 2(d)). This phenomenon arises from destructive interference in the far field emission along certain high symmetry directions. It occurs in lattices with multiple sites per unit cell [25] and it has been observed along the K- Γ -K directions of the first Bz in angle resolved electron spectroscopy measurements (ARPES) in graphene [26].

When the excitation intensity is increased we observe polariton condensation, as evidenced by the threshold in

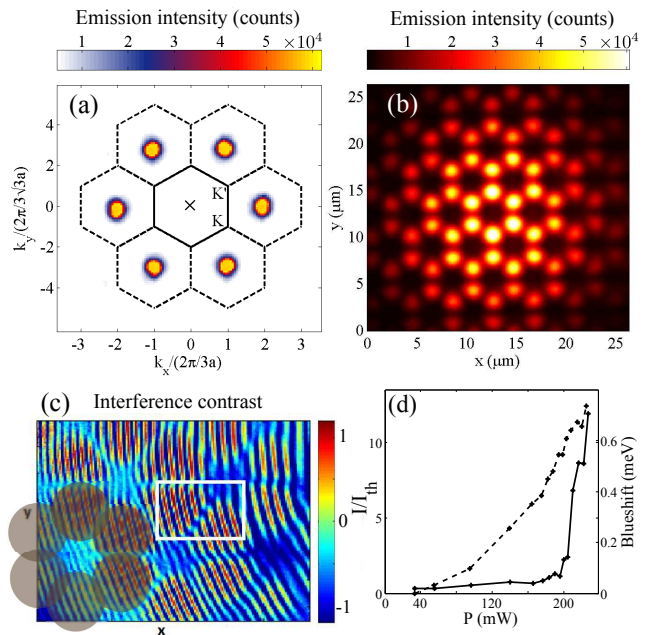


FIG. 3. (a) Photoluminescence emission in momentum space above the condensation threshold. The black solid/dashed line shows the first/second Brillouin zone. (b) Real space image of the condensed state. (c) Interference pattern obtained by overlapping the magnified image of a pillar and the total image. The position of six pillars is underlined with gray disks. (d) Total emitted intensity (black line) and blueshift of the polariton emission at the top of the π^* band (dashed line) as a function of excitation power.

the integrated emission intensity (Fig. 3(d)). The low value of the measured emission blueshift due to interactions between polaritons and uncondensed excitons (see Fig. 3(d)) certifies that the system remains in the strong coupling regime across the threshold [27]. Moreover the emission spectrum collapses into a single emission line, and extended spatial coherence builds up. By monitoring the energy resolved emitted intensity across the condensation threshold, we observe that condensation takes place at the top of the π^* band (the state marked with an arrow in Fig. 2(b)). This state is located at the Γ point (center of the Bzs), as observed in the momentum space measurement shown in Fig. 3(a). The far field destructive interference discussed above results in the absence of emission from the center of the first Bz, marked by a cross in Fig. 3(a).

The real space emission of the condensate is shown in Fig. 3(b), with maxima centered on the pillars as expected for a state arising from the hybridization of S states. By performing an interferometric measurement, we extract the phase structure. We proceed as follows: we magnify the image of one pillar, and make it interfere on the CCD with an image of the whole excited region [28]. The normalized interference pattern, without any energy selection, is shown in Fig. 3(c) above the

condensation threshold. We observe the appearance of spontaneous coherence over the whole size of the pump beam (around 30 pillars). At the intersection between two adjacent pillars (white square in Fig. 3(c)) the fringes are shifted by half a period. This shows that there is a π phase shift between adjacent pillars, as expected for the antisymmetric wavefunctions in the antibonding π^* band. Note that condensation does not take place in the ground state. This feature arises from the out of equilibrium nature of polaritons in which the steady state is fixed by the interplay between pump, relaxation and decay. The antibonding mode at the Γ point favors condensation due to three features that result in the accumulation of particles in that state: (i) its negative effective mass; (ii) its slightly longer lifetime related to the antisymmetric character of the state [29]; (iii) the lower non-radiative recombination rate due to the vanishing polariton density which vanishes at the constrictions between pillars.

We have shown that the two S bands mimic the graphene π and π^* bands. But the honeycomb lattice contains more than graphene physics if higher orbital modes are available. In the polariton honeycomb lattice, the coupling between P modes of the pillars leads to four energy bands which appear above the two S bands, separated by a gap of about 0.7 meV (see Fig. 1(d)). A closer look to the P bands in Fig. 1(d), shown in more details in Fig. 4(a), reveals that the lowest one is non dispersive. Non dispersive bands, also named flat bands, are characterized by an infinite effective mass and, consequently, a vanishing kinetic energy. In this situation, one can show that all states are localized without any interactions [30]. Moreover weak interactions have been predicted to give rise to strongly correlated phases in a lossless system [31, 32]. In order to understand the origin of the flat bands, one can extend the usual tight-binding treatment to P states with a Hamiltonian of the form [31]

$$\hat{H} = - \sum_{\langle i,j \rangle} \left[t_{\parallel} (\hat{\psi}_i^{\dagger} \cdot e_{ij}^{(L)}) (e_{ij}^{(L)\dagger} \cdot \hat{\psi}_j) + t_{\perp} (\hat{\psi}_i^{\dagger} \cdot e_{ij}^{(T)}) (e_{ij}^{(T)\dagger} \cdot \hat{\psi}_j) + \text{H.c.} \right] \quad (3)$$

For each ij link, the $e_{ij}^{(L,T)}$ unit vectors are directed respectively along and orthogonally to the link direction. In the Hamiltonian, they serve to extract the projections of the P state respectively along and orthogonal to the link: The t_{\parallel} amplitude then describes hopping between P states with main lobes located along the link, while t_{\perp} describes the (typically much weaker) hopping between states with lobes located sideways to the link. In the limiting case where $t_{\perp} = 0$ meV and $t_{\parallel} = -1$ meV, the eigenstates of Eq. 3 give rise to four energy bands plotted in Fig. 4(c). The two extreme bands are completely flat, the two intermediate ones are dispersive and intersecting

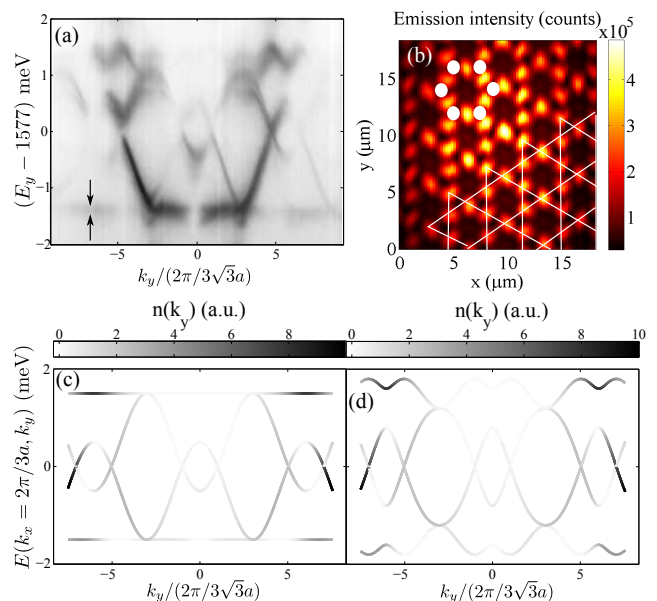


FIG. 4. (a) Zoom on the four P bands shown in Fig. 1(d). (b) Real space image integrated in energy over the flatband, marked with two arrows in (a). The center of six pillars are shown in white disks. The Kagome geometry of the emission lobes is underlined with white lines. (c) and (d) show the calculated energy dispersion along the $k_x = 2\pi/3a$ line (same direction as in (a)) from the Hamiltonian given in Eq. 3 for $t_{\parallel} = -1$ meV and $t_{\perp} = 0$ meV (c) and $t_{\perp} = 0.2$ meV (d). The color scale indicates the squared amplitude of the wavefunction

linearly. For those parameters, this model describes well the lower bands observed in the experiment (Fig. 4(a)). However one can see in Fig. 4(a) that the higher energy band is modulated. This behavior can be explained by allowing for a weak hopping also for the P states orthogonal to the link. Indeed in the case where $t_{\perp} = 0.2$ meV and $t_{\parallel} = -1$ meV, the tight-binding result is plotted in Fig. 4(d) where the two extreme bands are no longer flat. The band structure reported in Fig. 4(a) can then be understood assuming that t_{\perp} increases with the energy, resulting in a flat band ($t_{\perp} \simeq 0$) at low energy and a dispersive band ($t_{\perp} \simeq 0.2$ meV) at higher energy. Indeed, the tunneling probability varies exponentially with the barrier height relative to the state, and thus increases strongly for higher energy states. A numerical simulation of the 2D Schrödinger equation reproduces well the observed dispersion [33]. Finally Fig. 4(b) shows the real space mode corresponding to the flat band. We see that intensity maxima sit between the pillars, thus arranged in a Kagome lattice (underlined with white lines in Fig. 4(b)). Such a geometry is well known to give rise to flat bands due to the high degree of frustration in the system.

In summary, we have implemented a system which allows direct optical access to the basic properties of engineered lattices as demonstrated by the straightforward

observation of Dirac cones in a honeycomb geometry. These results demonstrate the potential of our system over previous experiments using cold atoms in optical lattices or other photonic devices, where only indirect evidence of the honeycomb lattice physics was obtained [8]. The position, shape and size of each lattice site can be controlled at will during fabrication, opening the way to study a wide range of intriguing effects, like disorder, Klein tunneling at a potential step [6], the geometrical Berry curvature of the bands [34] and the topological physics in the presence of synthetic gauge fields [14]. Additionally, the observation of a non dispersive band stemming from the coupling between the first excited modes of the pillars opens the way to the investigation of the rich interplay between frustration, dispersion and interactions in such flat bands [31, 32].

This work was supported by the French RENATECH, the ANR-11-BS10-001 contract "QUANDYDE", the RTRA Triangle de la Physique (contract "Bose-flow1D"), the FP7 ITNs "Clermont4" (235114), the FP7 IRSES "Polaphen" (246912), the POLATOM ESF Network, the Labex Nanosacly and the ERC (Honeyopol and QGBE).

-
- [1] I. Bloch and W. Zwerger, *Rev. of Mod. Phys.* **80**, 885 (2008).
- [2] A. Szameit and S. Nolte, *J. of Phys. B* **43**, 163001 (2010).
- [3] I. Carusotto and C. Ciuti, *Rev. of Mod. Phys.* **85**, 299 (2013).
- [4] A. K. Geim and K. S. Novoselov, *Nature Mat.* **6**, 183 (2007).
- [5] A. H. Castro Neto, N. M. R. Peres, K. S. Novoselov, and A. K. Geim, *Rev. of Mod. Phys.* **81**, 109 (2009).
- [6] P. E. Allain and J. N. Fuchs, *Eur. Phys. J. B* **83**, 301 (2011).
- [7] H. Suzuura and T. Ando, *Phys. Rev. Lett.* **89**, 266603 (2002).
- [8] M. Polini, F. Guinea, M. Lewenstein, H. C. Manoharan, and V. Pellegrini, *Nature Nano.* **8**, 625 (2013).
- [9] P. Soltan-Panahi, J. Struck, P. Hauke, A. Bick, W. Plenkers, G. Meineke, C. Becker, P. Windpassinger, M. Lewenstein, and K. Sengstock, *Nature Phys.* **7**, 434 (2011).
- [10] L. Tarruell, D. Greif, T. Uehlinger, G. Jotzu, and T. Esslinger, *Nature (London)* **483**, 302 (2012).
- [11] G. De Simoni, A. Singha, M. Gibertini, B. Karmakar, M. Polini, V. Piazza, L. N. Pfeiffer, K. W. West, F. Beltram, and V. Pellegrini, *Appl. Phys. Lett.* **97**, 132113 (2010).
- [12] K. K. Gomes, W. Mar, W. Ko, F. Guinea, and H. C. Manoharan, *Nature (London)* **483**, 306 (2012).
- [13] O. Peleg, G. Bartal, B. Freedman, O. Manela, M. Segev, and D.N. Christodoulides, *Phys. Rev. Lett.* **98**, 103901 (2007).
- [14] M. C. Rechtsman, J. M. Zeuner, A. Tünnermann, S. Nolte, M. Segev, and A. Szameit, *Nature Phot.* **7**, 153 (2012).
- [15] M. C. Rechtsman, J. M. Zeuner, Y. Plotnik, Y. Lumer, D. Podolsky, F. Dreisow, S. Nolte, M. Segev, and A. Szameit, *Nature (London)* **496**, 196 (2013).
- [16] S. Bittner, B. Dietz, M. Miski-Oglu, P. Oria Iriarte, A. Richter, and F. Schäfer, *Phys. Rev. B* **82**, 014301 (2010).
- [17] M. Bellec, U. Kuhl, G. Montambaux, and F. Mortesagne, *Phys. Rev. B* **88**, 115437 (2013).
- [18] E. A. Cerda-Méndez, D. N. Krizhanovskii, M. Wouters, R. Bradley, K. Biermann, K. Guda, R. Hey, P. V. Santos, D. Sarkar, and M. S. Skolnick, *Phys. Rev. Lett.* **105**, 116402 (2010).
- [19] E. A. Cerda-Méndez, D. N. Krizhanovskii, K. Biermann, R. Hey, M. S. Skolnick, and P. V. Santos, *Phys. Rev. B* **86**, 100301 (2012).
- [20] N. Y. Kim, K. Kusudo, C. Wu, N. Masumoto, A. Löffler, S. Höfling, N. Kumada, L. Worschech, A. Forchel, and Y. Yamamoto, *Nature Phys.* **7**, 681 (2011).
- [21] N. Y. Kim, K. Kusudo, A. Löffler, S. Höfling, A. Forchel, and Y. Yamamoto, *New J. of Phys.* **15**, 035032 (2013).
- [22] K. Kusudo, N. Y. Kim, A. Löffler, S. Höfling, A. Forchel, and Y. Yamamoto, *Phys. Rev. B* **87**, 214503 (2013).
- [23] A. Dousse, J. Suffczyński, A. Beveratos, O. Krebs, A. Lemaître, I. Sagnes, J. Bloch, P. Voisin, and P. Senellart, *Nature (London)* **466**, 217 (2010).
- [24] M. Galbiati, L. Ferrier, D. D. Solnyshkov, D. Tanese, E. Wertz, A. Amo, M. Abbarchi, P. Senellart, I. Sagnes, A. Lemaître, E. Galopin, G. Malpuech, and J. Bloch, *Phys. Rev. Lett.* **108**, 126403 (2012).
- [25] E.L. Shirley, L.J. Terminello, A. Santoni, and F.J. Himpfel, *Phys. Rev. B* **51**, 13614 (1995).
- [26] A. Bostwick, T. Ohta, T. Seyller, K. Horn, and E. Rotenberg, *Nature Phys.* **3**, 36 (2006).
- [27] L. Ferrier, E. Wertz, R. Johne, D. D. Solnyshkov, P. Senellart, I. Sagnes, A. Lemaître, G. Malpuech, and J. Bloch, *Phys. Rev. Lett.* **106**, 126401 (2011).
- [28] F. Manni, K.G. Lagoudakis, R. André, M. Wouters, and B. Deveaud, *Phys. Rev. Lett.* **109**, 150409 (2012).
- [29] I. L. Aleiner, B. L. Altshuler, and Y. G. Rubo, *Phys. Rev. B* **85**, 121301 (2012).
- [30] A. Petrescu, A. A. Houck, and K. Le Hur, *Phys. Rev. A* **86**, 053804 (2012).
- [31] S. D. Huber and E. Altman, *Phys. Rev. B* **82**, 184502 (2010).
- [32] C. Wu, D. Bergman, L. Balents, and S. Das Sarma, *Phys. Rev. Lett.* **99**, 070401 (2007).
- [33] See supplementary materials XXX.
- [34] T. Ozawa and I. Carusotto, (2013), arXiv:1307.6650 .

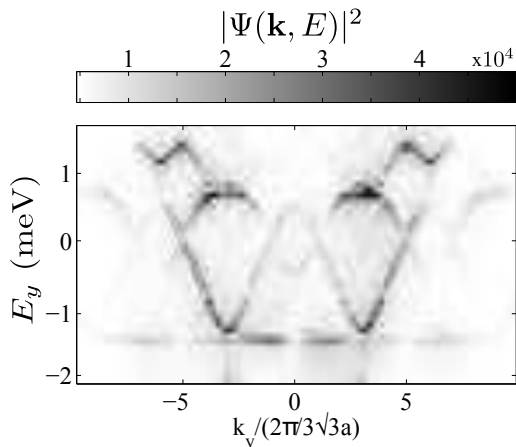


FIG. 5. Simulation of $|\Psi(\mathbf{k}, E)|^2$ along the same momentum space direction as Fig. 4(a) in the main text, based on the solution of Eq. 4.

In order to reproduce the experimental data shown in Fig. 4(a), we have performed a 2D Schrödinger equation simulation for polaritons in the low density limit. Since the S and P bands are located close to the bottom of the lower polariton branch, we use the effective mass approximation:

$$i\hbar\partial_t\Psi = -\frac{\hbar^2}{2m}\Delta\Psi + \left(U - \frac{i\hbar}{2\tau}\right)\Psi + P_0 e^{-\frac{(t-t_0)^2}{\tau_0^2}} e^{-\frac{(\mathbf{r}-\mathbf{r}_0)^2}{\sigma^2}} e^{-i\omega t}. \quad (4)$$

Here m is the polariton mass, $\tau = 30$ ps is the polariton lifetime, and U is the external potential describing

the etched honeycomb lattice shown in Fig. 1(c). In our simulation we use a rectangular sample made out of coupled micropillars of round geometry and same dimension as in the experiment, arranged in a lattice with 16 by 16 unit cells. The height of the polariton confining potential in the micropillars was taken 20 meV. The last term of Eq. (1) simulates a pulsed probe that will excite the different eigenstates of the Schrödinger equation, thus allowing their visualization. P_0 is the amplitude of the probe, arriving at the sample at t_0 , $\tau_0 = 0.2$ ps is the pulse duration, $\sigma = 0.7 \mu\text{m}$ the spot size. Using a short pulse and a small spot allows exciting several bands of the dispersion at the same time. \mathbf{r}_0 is the pump location (center of the sample, which does not correspond to the center of a particular pillar) and ω is the pump central frequency, centered 4 meV above the bottom of the lower polariton branch to mainly excite the P band multiplet. Let us note that the probe pulse excites different parts of the dispersion with different efficiency, depending on their symmetry.

The Schrödinger equation is then integrated over time for 100 ps with a spatial grid 512x512 (the size of the grid is $80' \times 80\mu\text{m}$) using a NVIDIA graphic card. The solution of the equation $\Psi(\mathbf{r}, t)$ is then Fourier-transformed over time and space to obtain the dispersion $|\Psi(\mathbf{k}, E)|^2$. The result is shown in Fig 5 along the same momentum-space direction as in Fig. 4(a). The simulation is in excellent quantitative agreement with the experimental observation: the lowest P band is indeed flat, while the upper band is dispersive. The full 2D model reproduces this behavior correctly, because it automatically takes into account the exponential increase with energy of the tunneling rate of the P states of the individual pillars, as explained in the main text and illustrated by the tight-binding model calculations.